High-performance solid-state flexible supercapacitor based on reduced graphene oxide/hierarchical core-shell Ag nanowire@NiAl layered double hydroxide film electrode

Lei Li[a], Kwan San Hui[b*], Kwun Nam Hui[c*], Tengfei Zhang[a], Jianjian Fu[a], and Young-Rae Cho[a*]

[a] School of Materials Science and Engineering, Pusan National University, San 30 Jangjeon-dong, Geumjeong-gu, Busan 609-735, Republic of Korea

[b] School of Mathematics, University of East Anglia, Norwich, NR4 7TJ, United Kingdom

[c] Institute of Applied Physics and Materials Engineering, University of Macau, Avenida da Universidade, Macau, China

*Corresponding author:

E-mail: k.hui@uea.ac.uk (Kwan San Hui)

E-mail: bizhui@umac.mo (Kwun Nam Hui)

E-mail: yescho@pusan.ac.kr (Young-Rae Cho)

Abstract

All-solid-state flexible supercapacitor (AFSC) is a promising energy storage device due to its high flexibility, security, and environmental friendliness. However, high electrical resistance and low specific capacitance of electrodes limit its application for potential portable electronic devices. In this study, we design a novel hybrid film electrode composed of reduced graphene oxide (rGO)/silver nanowire (Ag NW)@nickel aluminum layered double hydroxide (NiAl LDH; herein, GAL) possessing high electrochemical performance by using hydrothermal and vacuum filtration techniques. The Ag NW@NiAl LDH (AL) composites with hierarchical core-shell structure are utilized to increase electroactive surface area and improve electrical conductivity, while the rGO nanosheets serve as a prominent carbon material with outstanding electrical conductivity and mechanical flexibility. The freestanding GAL electrode shows high specific capacitance of 1148 F g^{-1} at 1 A g^{-1} compared with that of rGO/NiAl LDH (GL) of 765.2 F g^{-1} at 1 A g^{-1}. The bind-free symmetric AFSC device is prepared using GAL hybrid film as electrodes and PVA-KOH as solid-state gel electrolyte. Meanwhile, the GAL//GAL AFSC device delivers a superior specific capacitance of 127.2 F g^{-1} at 1 A g^{-1}, a high energy density of 35.75 mWh cm^{-3} at a power density of 1.01 W cm^{-3}, and great cycling ability of 83.2% over 10000 cycles. This study introduces a novel design of flexible electrode structure for advanced energy storage applications.

Keywords: Silver nanowire; Layered double hydroxide; Reduced graphene oxide; Hybrid film; All-solid-state supercapacitor

1. Introduction

With the rapid development of electronic technology, wearable and flexible devices such as roll-up displays, biomedical sensors, and wearable devices, have drawn considerable attention [1-5]. Developing high energy density flexible supercapacitors (FSCs) hold the promise to provide a safe, fast charge/discharge rate, and long-life flexible energy storage devices [6-8]. Current research has focused on developing flexible film electrode possessing high electrical conductivity, high mechanical flexibility, and superior electrochemical performance for achieving high energy density FSCs [9-13]. To date, electrodes of high-performance FSCs are mainly composed of carbonaceous materials such as carbon nanotube (CNT) [14-16], graphene [17-19] and CNT/graphene hybrid [20] due to their distinct properties of high conductivity and mechanical flexibility [21-23]. However, the CNT/graphene-based electric double-layer capacitor (EDLC) possesses low specific capacitance due to its intrinsic double-layer charge storage mechanism, which relies on the electrostatic attraction of electrolyte ions and charges at the electrode surface [24].

Accordingly, hybridizing pseudocapacitive metal oxide materials with CNT and/or graphene has been extensively studied to increase the specific capacitance and energy density of film electrodes [25-29]. However, fabricating flexible electrodes with high electrical conductivity and mechanical flexibility remains a challenge despite the use of the abovementioned superior carbonaceous materials. Recently, one-dimensional (1D) silver nanowires (Ag NWs) have been extensively studied as alternative conducting electrode materials in the electrochemical field due to their high electrical conductivity and mechanical flexibility [30, 31]. Particularly, the embedment of Ag NWs in the carbonaceous matrix exhibits remarkably electrical conductivity and mechanical flexibility. Chen et al. reported the embedment of 1D Ag NWs in the matrix of chemical vapor deposition (CVD) graphene to enhance the

electrical conductivity of Ag NW/CVD graphene film electrodes. The superior electrical conductivity of 3189 S cm^{-1} was obtained in the optimized 50 wt% Ag NW/CVD graphene film [32]. However, few research has utilized 1D Ag NWs as the backbone of pseudocapacitive materials, such as transition metal oxide/hydroxides as an advanced electrode for FSCs. Hydrotalcite-like layered double hydroxides (LDH) have been demonstrated as promising pseudocapacitive materials due to their versatility in the matrix composition, high redox activity, low cost, and environmental benignity [33-35]. Generally, the typical formula for LDH is $[M_{1-x}^{2+}M_x^{3+}(OH)_2](A^{n-})_{x/n}\cdot mH_2O$, where M^{2+} indicates divalent cations such as Co^{2+}, Cu^{2+}, Ni^{2+}, Zn^{2+}, and Mg^{2+}; M^{3+} is a trivalent cation that includes Mn^{3+}, Al^{3+}, Cr^{3+}, and Fe^{3+}; and A^{n-} is stand for the interlayer exchangeable anion such as SO^{4-}, OH^{-}, NO^{3-}[35].

In this study, a novel architecture film electrode composed of reduced graphene oxide (rGO)/ silver nanowire (Ag NW)@nickel aluminum layered double hydroxide (NiAl LDH; herein GAL) hybrid film is successfully fabricated and applied as a film electrode for all-solid-state flexible supercapacitor (AFSC) device. The ultrathin and lamellate NiAl LDH nanosheets are grown on the Ag NWs to form a hierarchical core-shell composite by a facile hydrothermal method. Then, the core-shell Ag NW@NiAl LDH (AL) composite are assembled with rGO via the vacuum filtration technique to form the GAL hybrid film. In comparsion with reported LDH-based composites, such as LDH/CNT [36], LDH/carbon nanoparticles, and LDH/carbon nanofibers [37], the GAL architecture offers the following intriguing features [38-41]: (1) 1D Ag NW offers excellent electrical conductivity to facilitate the transport of electron; (2) ultrathin porous NiAl LDH nanosheet surfaces grown along 1D Ag NW provide the effective electrolyte diffusion and prevent the aggregation of NiAl LDH nanosheets; (3) highly conductive and mechanically flexible rGO buffers the volume expansion of NiAl-

LDH; and (4) AL core-shell improves the specific capacitance performance due to its pseudocapacitive characteristic and acts as a spacer to prevent the aggregation of rGO nanosheets. The GAL hybrid film displays a remarkable specific capacitance of 1148 F g^{-1} at 1 A g^{-1} compared with the rGO/NiAl LDH (GL) of 765.2 F g^{-1} at 1 A g^{-1} and records a favorable cycling stability of 77.2% capacitance retention after 10000 cycles at 5 A g^{-1}. A bind-free symmetric AFSC device is successfully prepared using GAL hybrid film as electrodes and PVA/KOH as solid-state gel electrolyte. The GAL//GAL AFSC device delivers a superior specific capacitance of 127.2 F g^{-1} at 1 A g^{-1}, a high volumetric energy density of 35.75 mWh cm^{-3} at a power density of 1.01 W cm^{-3}, and great cycling ability of 83.2% over 10000 cycles.

2. Experimental section

2.1. Synthesis of AL composites

Ag NWs were synthesized via a solvothermal method according to the reported literature [42]. AL composites were prepared through a typically hydrothermal method. Briefly, 0.003 mol of $Ni(NO_3)_2 \cdot 6H_2O$, 0.001 mol of $Al(NO_3)_3 \cdot 9H_2O$, and 0.5 mg ml^{-1} of Ag NWs were dispersed into 30 ml deionized (DI) water under ultrasonication for 15 min. Then, 0.04 mol of urea was added into the as-prepared solution and stirred for another 15 min. The resultant mixture solution was transferred to a 50 mL Teflon-lined stainless-steel autoclave and kept at a temperature at 95 ℃ for 24 h. After crystallization, the generated precipitates were washed with ethanol and DI water, centrifuged, and dried at 60 °C for 12 h in a vacuum oven.

2.2. Preparation of GAL hybrid film

Graphene oxide (GO) was prepared from graphite powder via a modified Hummers method [43, 44]. The obtained GO powder (10 mg) was dispersed in 20 ml DI water under

ultrasonication for 30 min to create a homogeneous aqueous suspension. Subsequently, the brown color suspension was centrifuged at 3000 rpm for 30 min to remove any unexfoliated GO. To chemically reduce the GO, 280 µl of ammonia and 20 µl of hydrazine were added to the GO suspension with rapid stirring for several minutes. The suspension was then transferred into a glass vial and placed in water bath at 95 °C for 1h. The obtained black rGO suspension was mixed with 20 ml AL suspensions After 2 h, the GAL hybrid film was fabricated by vacuum filtration method with a polytetrafluoroethylene Millipore filter (0.2 µm pore size, 47 mm in diameter). During the process, the prepared GAL suspension was added to the filtration system for 5 times (20 ml each time). Finally, the freestanding GAL composite film with thickness of 8 µm was obtained after being peeled off from the filter carefully.

2.3. Fabrication of AFSC device

Solid-state symmetric supercapacitors were assembled using GAL as the positive and negative electrodes with PVA/KOH gel as a solid electrolyte. In the assembly of GAL//GAL flexible symmetric devices, the area of the GAL electrode was 1 cm × 2 cm. The mass loading of the GAL was 1 mg cm^{-2}. Gold-coated polyethylene terephthalate (Au-PET) membranes were used as conductive plates. The PVA/KOH electrolyte was prepared as follows. PVA (3.0 g) and KOH (3.0 g) were dissolved in 30 mL of water with vigorous and continuous stirring at 85 °C until the solution becomes clear. Before the device assembly, electrodes were soaked in the PVA/KOH sol for 5 min and then allowed to solidify at room temperature for 6 h. Finally, they were assembled together under pressing and remained at 45 °C for 12 h to remove excess water.

2.4. Materials characterization

X-ray diffraction (XRD) patterns were recorded using a Bruker D8 Advance X-ray diffractometer with Ni-filtered Cu Kα radiation (λ = 1.5406 Å) at a voltage of 40 kV and current of 200 mA. The composition and valence states of the prepared samples were analyzed by X-ray photoelectron spectroscopy (XPS, VG Scientific ESCALAB250). The instrument was calibrated to the carbon peak C 1s at 284.6 eV. Field-emission scanning electron microscopy images were acquired using Hitachi S-4800. Transmission electron microscopy (TEM) images were obtained using Talos F200 X. Scanning TEM with energy-dispersive X-ray spectroscopy (EDS, Talos F200 X) mapping was performed to identify the distributions of C, O, Ni, Ag, and Al.

2.5. Electrochemical measurements

Electrochemical performance was evaluated by an electrochemical workstation (IviumNstat) with a 6 M KOH electrolyte. A three-electrode system with a GAL hybrid film (1 cm × 2 cm), a saturated calomel electrode (SCE, Hg/Hg_2Cl_2) and a platinum foil were used as working, reference, and counter electrodes, respectively. Cyclic voltammetry (CV) was measured with various scan rates at a potential window from 0 V to 0.6 V. Galvanostatic charge–discharge (GCD) was conducted with various current densities at a potential window from 0 V to 0.5 V. Electrochemical impedance spectroscopy (EIS) test was evaluated at a frequency range from 100 kHz to 0.01 Hz at the open circuit potential with an AC potential amplitude of 5 mV. The gravimetric specific capacitance (C_g) was calculated by GCD tests by using the following equation:

$$C_g = (I \times \Delta t)/(\Delta V \times m) \quad (1)$$

where I is the discharge current (A), Δt is the discharge time (s), m is the mass of the active

material in the electrode (g), and ΔV is the total potential deviation (V). To further evaluate the performance of the AFSC device, specific capacitance is calculated in Eq. (1) based on the total mass of two electrodes. The gravimetric energy density (E_g) and power density (P_g) were calculated using the following equations:

$$E_g = \frac{1}{2} \times C_g \times \Delta V^2 \quad (2)$$

$$P_g = E_g / \Delta t \quad (3)$$

where ΔV (V) is the device voltage and Δt (s) is the device discharge time. Moreover, the volumetric energy density (E_v) and power density (P_v) were calculated according to the following equations [45]:

$$E_v = \rho E_g \quad (4)$$

$$P_v = \rho P_g \quad (5)$$

Where ρ is the density of the hybrid film, which was calculated by the following equation:

$$\rho = m/(S \times d) \quad (6)$$

where m (g) is the mass of the hybrid film, S (cm^2) is the area and d (cm) is the thickness of the hybrid film.

3. Results and discussion

3.1. Material characterization

Fig. 1a shows the schematic of the core-shell AL composites. In the synthesis process, long and thin 1D Ag NWs were used as the high conductivity 1D core for the growth of NiAl-LDH. During the hydrothermal reaction, urea was first hydrolyzed to provide OH^- and CO_3^{2-} for the precipitation of Ni^{2+} and Al^{3+} to form NiAl LDH along the Ag NWs surface [46, 47]. The detailed chemical reactions of AL can be expressed as follows [48]:

$$NH_3 + H_2O \rightarrow NH_4^+ + OH^- \quad (7)$$

$$6Ni^{2+} + 2Al^{3+} + 0.5CO_3^{2-} + 17OH^- + 4H_2O \rightarrow Ni_6Al_2(OH)_{16}(CO_3, OH) \cdot 4H_2O \quad (8)$$

The crystal structures of the Ag NW and AL were measured by XRD measurement, as shown in Fig. 1b. In the XRD pattern of NiAl LDH, well-defined diffraction peaks at 11.7°, 23.5°, 35.1°, 39.5°, 61.2° and 62.3° are indexed as (003), (006), (012), (015), (018), (110), and (113) rhombohedral phase of NiAl LDH (JCPDS 15-0087) with the R_{3m} space group [49]. Conversely, the XRD results of AL composites reveal the presence of XRD peaks of NiAl LDH and Ag NW that are indexed to the (111), (200), and (220) crystal planes of Ag (JCPDS 65-2871) This result further confirms that the AL core-shell composites are successfully synthesized by the hydrothermal method. Scanning electron microscopy (SEM) was conducted to study the morphology of the AL composites. Fig. 1c shows the SEM images of as-prepared 1D Ag NWs with different magnifications at 5 μm and 500 nm. The minimal diameter of the Ag NW is approximately 200 nm, which indicates the high uniformity of the Ag NW. Fig. 1d shows the as-synthesized AL composites composed of vertically grown NiAl LDH nanosheets along the surface of Ag NWs, revealing a highly hierarchical core-shell structure. Such core-shell structure enables efficient electroactive surface area for Faradaic redox reactions and is expected to shorten the diffusion and migration paths of the electrolyte ions.

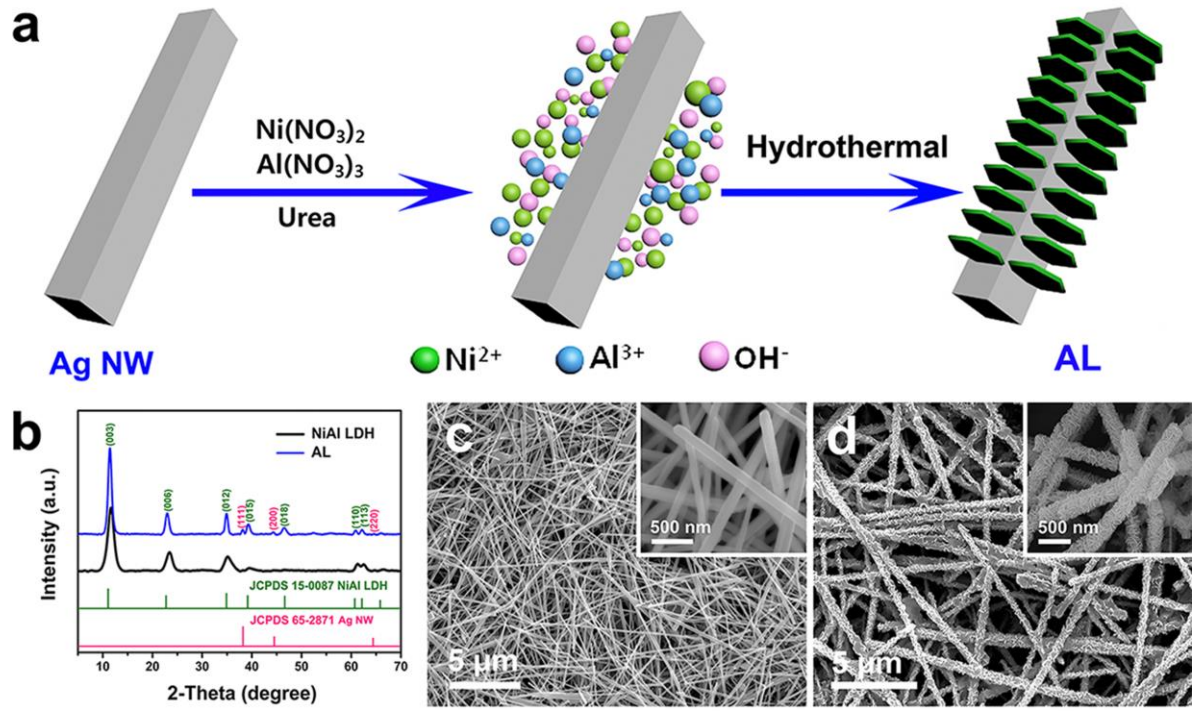

Fig. 1. (a) Schematic illustration of the formation process of the hierarchical core-shell AL composites; (b) XRD patterns of NiAl LDH and AL composites; SEM images of (c) Ag NWs and (d) AL composites.

The schematic of the preparation process of the GAL hybrid film is shown in Fig. 2a. In the process, the rGO and AL composites were dispersed in DI water under ultrasonication to obtain the homogeneous suspensions. The GAL hybrid film was then formed by a vacuum filtration of the mixture of the rGO and AL suspensions. The XRD patterns of the rGO and GAL hybrid films are shown in Fig. 2b. The results show that rGO and GAL display a broad reflection peak at 24.3° , indicating the explicit characteristic of poor ordering of rGO sheets along their stacking direction [50, 51]. Furthermore, the distinct peaks at 11.7° , 23.4° , 35.2° , 39.6° and 47.1° are observed in the GAL hybrid film, which corresponds to the typical NiAl LDH peaks. To demonstrate the dispersibility of the rGO and AL in aqueous solutions, the Tyndall effect of the dispersions was studied (Fig. 2c). Distinct red light paths

are clearly shown in the rGO, and AL aqueous solutions, which indicate the typical colloidal nature and remarkable stability of the rGO and AL dispersions [52]. The surface morphology and cross-section SEM images of the rGO and GAL hybrid films were investigated by SEM. Fig. 2d illustrates the flat surface of rGO film with a wrinkled edge. The cross-section SEM image reveals the rGO film composed of massive rGO nanosheets restacked together to form layers. By contrast, the GAL hybrid film composed of the rGO layers that are well separated with the introduction of AL composites resulted in clear spaces between rGO layers (Fig. 2e). To clearly observe the thickness of GAL hybrid film, Fig. S1 shows the cross section SEM image of GAL hybrid film, with thickness of 7.91 μm. This GAL architecture enables effective electrolyte diffusion between rGO layers and shortens diffusion paths to NiAl LDH, resulting in enhanced EDLC and pseudocapacitance.

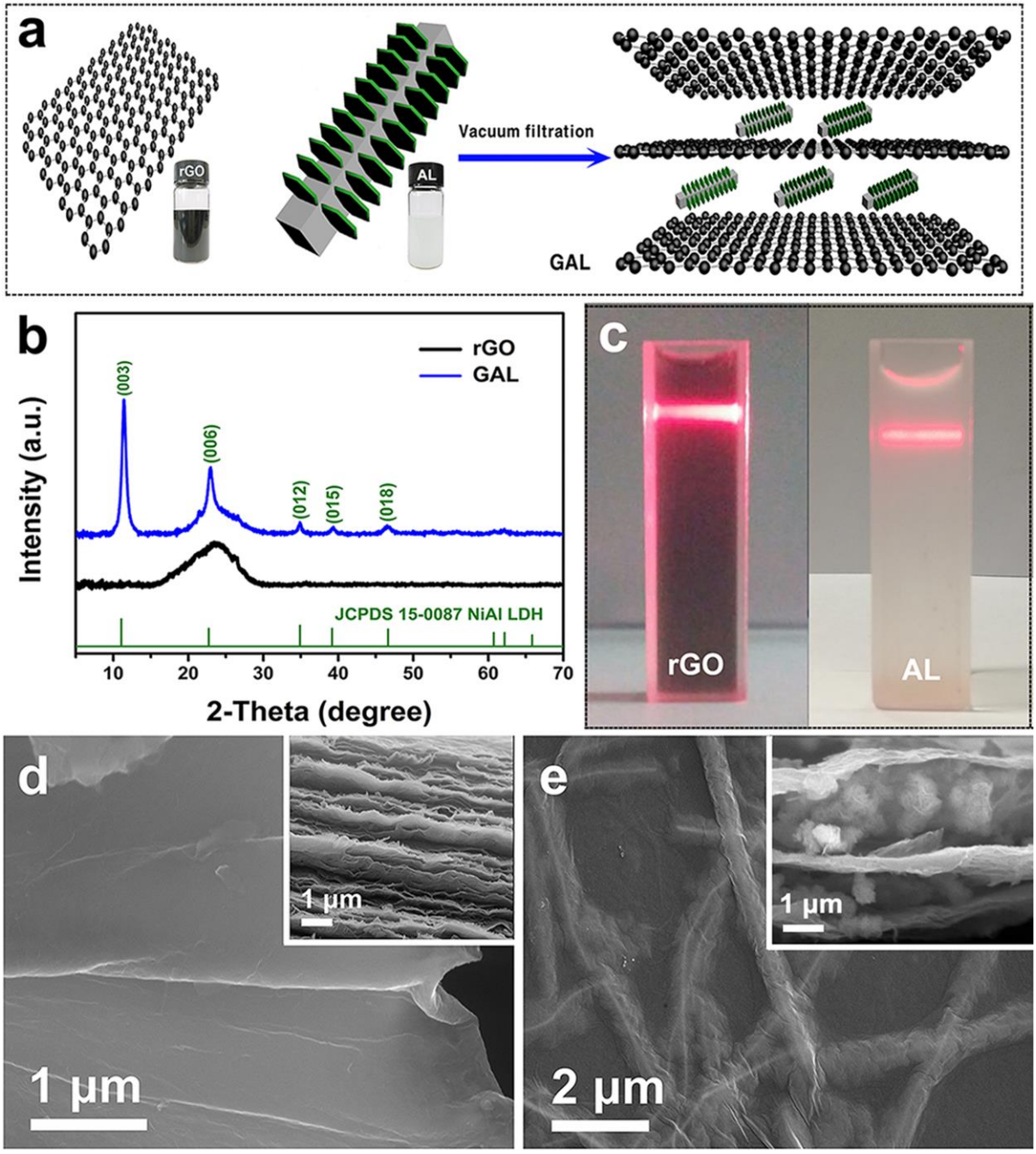

Fig. 2. (a) Schematic illustration of the GAL film; (b) XRD patterns of rGO and GAL film; (c) Tyndall effect illustration of rGO and AL composites dispersions; SEM and cross-sectional images of (d) rGO and (e) GAL film.

The microstructure of the GAL hybrid film was further evaluated by TEM. As shown in Fig. 3a-b and Fig. S2a, the surface of the Ag NWs is uniformly covered with the ultrathin NiAl

LDH nanosheets, signifying a perfect core-shell hierarchical structure. Notably, numerous thin and wrinkled rGO nanosheets were electrostatically attracted to AL composites resulting in a self-assembly of the GAL hybrid film. The self-assembly of AL composites and rGO was ascribed to the positively charged NiAl LDH surface [53] and the negatively charged rGO due to the ionization of the partial oxygen functional groups that were incompletely reduced [54]. The selected area electron diffraction (SAED) pattern (inset of Fig. 3c) reveals the well-defined diffraction rings corresponding to the (113) and (018) planes of NiAl LDH, indicating the polycrystalline structure of the LDH nanosheets. High-resolution TEM (HRTEM) image differentiated clearly the NiAl LDHs and rGO, as shown in Fig. 3d. The wrinkled rGO nanosheet depicts an explicit interlayer spacing of 0.345 nm, which indicates the typical graphene nature [55]. The (018) plane of NiAl LDH phase with an interlayer distance of 0.189 nm is observed in the HRTEM image, which matches well with the XRD results (Fig. 3e). To verify the spatial distribution of the chemical components of the AL composites, high-angle annular dark-field (HAADF) scanning TEM image of an AL composite structure and the corresponding EDS mapping analysis (Fig. 3f) were conducted. The EDS results reveal clearly the distinct distribution of Ni, Al, and Ag in the AL composites, which further confirms the well-defined core-shell structure with Ag NW core and NiAl LDH nanosheets. The HAADF mapping image of the GAL hybrid film showing the presence of Ni, Al, Ag, and C is shown in Fig S2b.

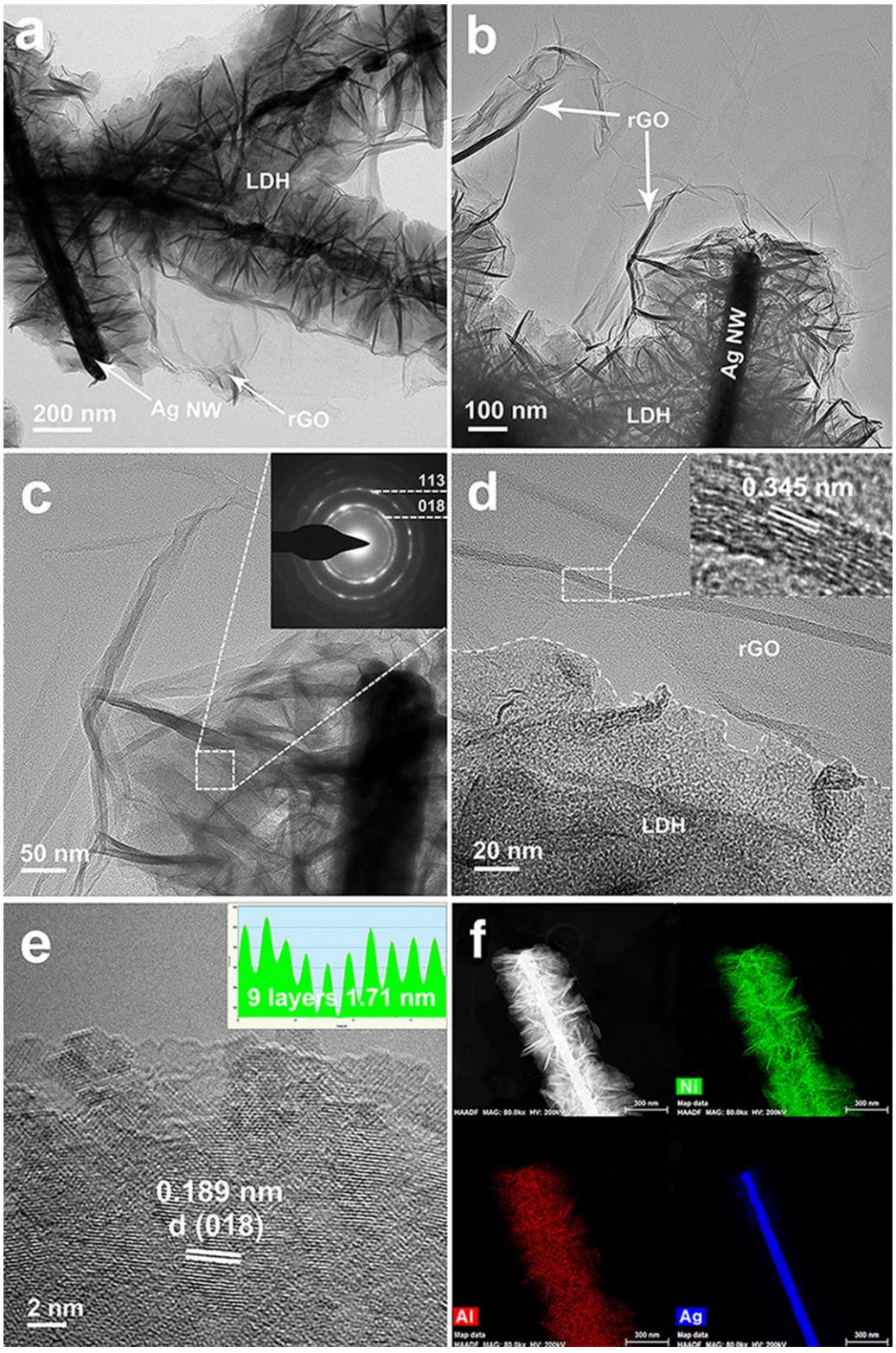

Fig. 3. (a, b, c) TEM images of GAL film with different magnifications; (inset in c) the corresponding SAED pattern of NiAl LDH in AL composites; HRTEM image of (d) GAL, (inset in d) rGO and (e) NiAl LDH; (f) Mapping results of AL composites.

XPS measurement was used to assess the surface chemical states of the GAL film. Fig. 4a shows the full XPS spectra of the GAL film, which is composed of Ni, Al, Ag, O and C. A close inspection reveals that Ni, Al, and Ag exhibit weaker peaks. This result is attributed to the few-nanometer electron escape depth of XPS measurement and the core-shell AL composites wrapped within the rGO sheets, resulting in weak XPS signal. Fig. 4b reveals a main peak of C 1s at approximately 284.6 eV, suggesting the graphitic sp2 carbon atoms. Meanwhile, two weak peaks are also exhibited at 286.5 eV and 288.4 eV, which are attributed to the presence of oxygenate groups (C–O and C=O) on the rGO sheets [56, 57]. The high-resolution XPS spectrum of Ni 2p (Fig. 4c) depicts two characteristic peaks at 856.2 eV and 874.1 eV with their shakeup satellites (indicated by "Sat"), corresponding to Ni $2p_{3/2}$ and Ni $2p_{1/2}$ spin-orbit doublets of the NiAl LDH, respectively; this result further confirmed the presence of Ni^{2+}.[48] The Ag 3d XPS spectrum (Fig. 4d) exhibits two peaks of Ag $3d_{5/2}$ and Ag $3d_{3/2}$ at the binding energies of 368.5 eV and 374.4 eV, indicating the presence of Ag metal inside the AL composites [58]. Furthermore, the O 1s spectrum is fitted by two peaks at 530.4 eV and 531.9 eV, which correspond to lattice oxygen and hydroxide group in the rGO sheets, respectively (Fig. S3) [59].

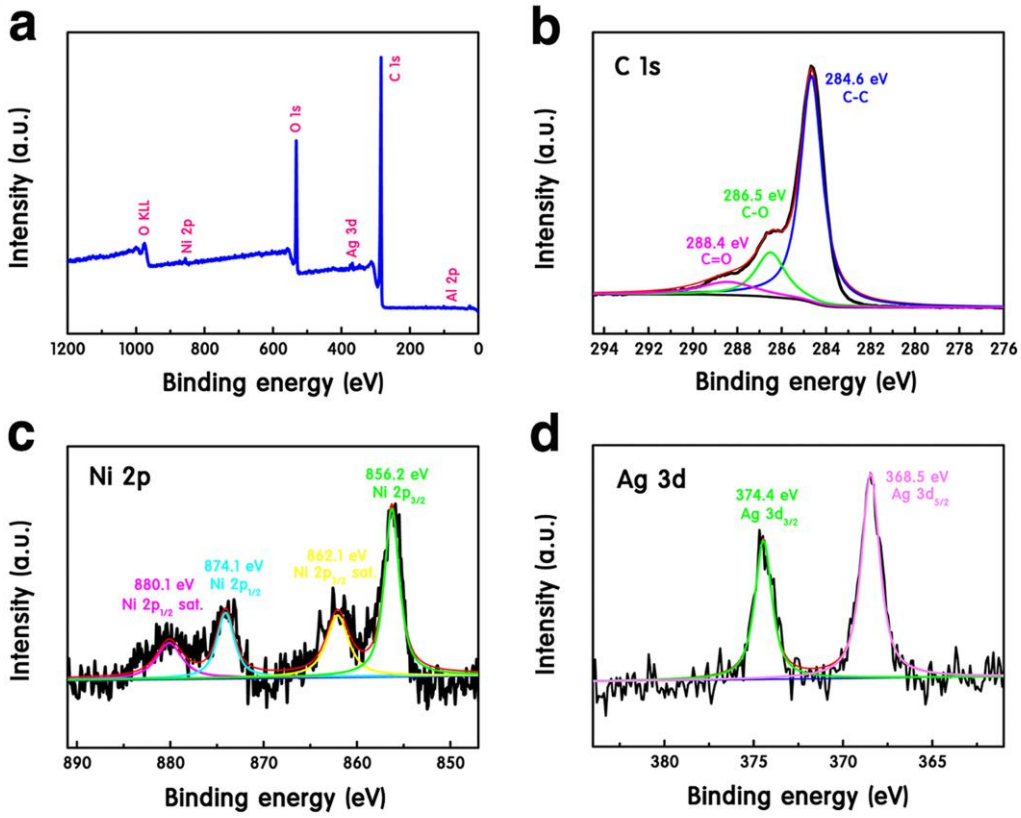

Fig. 4. XPS results of the GAL hybrid film: (a) full spectrum, (b) C 1s, (c) Ni 2p, and (d) Ag 3d.

3.2. Electrochemical characterization

The electrochemical performances of the freestanding GAL and GL electrodes were evaluated in a three-electrode system with 6 M KOH solution as the electrolyte (Fig. 5**)**. The GL film was tested as a reference compared with the GAL film. The CV curves of the GL and GAL film electrodes at a scan rate of 100 mV s^{-1} in the voltage range of 0–0.6 V (versus SCE) are shown in Fig. 5a. The results show that the GAL and GL electrodes present a pair of well-defined redox peaks attributed to the capacitive nature of the reversible redox reaction of Ni^{2+}/Ni^{3+} in alkaline electrolyte [60-62]. The redox reactions during the CV test are shown as follows:

$$Ni(OH)_2 + \ OH^- \leftrightarrow NiOOH + H_2O + e^- \quad (9)$$

Notably, the GAL electrode exhibits a higher current density and larger integral area than that of the GL electrode, revealing that GAL electrode has superior capacitive characteristics. This prominent electrochemical performance is attributed to the superior electrical conductivity of 1D Ag NW and the enhanced diffusion of electrolyte ions ascribed to the ultrathin NiAl LDH nanosheets [63] of the core-shell AL composites. Fig. S4a-b show the CV curves of the GAL and GL electrodes at various scan rates of 5, 10, 20, 30, 40, 50 and 100 m V s^{-1}. With an increase in scan rate from 5 m V s^{-1} to 100 m V s^{-1}, the clear shape of the redox peaks are maintained with a small shift, illustrating the small diffusion resistance of the electrode material and good rate capability [2, 64]. In addition, the correlation between the cathodic peak current and the square roots of the scan rates ($v^{1/2}$) of the GAL and GL electrodes is shown in Fig. 5b. The GAL and GL electrodes exhibit a linear relationship between the cathodic peak current and $v^{1/2}$, indicating a diffusion-controlled process [65]. Accordingly, the diffusion coefficient (D) of OH^- ion is calculated using Randles–Sevcik equation, as shown as follows [66]:

$$I_p = 2.69 \times 10^5 \times n^{3/2} \times A \times \sqrt{D} \times C \times \sqrt{v} \quad (10)$$

$$D_{GAL}/D_{GL} = [D(I_p/v^{1/2})_{GAL}/D(I_p/v^{1/2})_{GL}]^2 = (13.15/10.01)^2 = 1.73 \quad (11)$$

where I_p is the peak current, n is the number of electrons involved in the reaction, A is the surface area of the electrode, D is the diffusion coefficient of the electrode material, C is the proton concentration, and v is the scanning rate. The diffusion coefficient of the GAL electrode (D_{GAL}) is approximately 1.73 times larger than that of the GL electrode (D_{GL}), indicating its higher ion mobility.

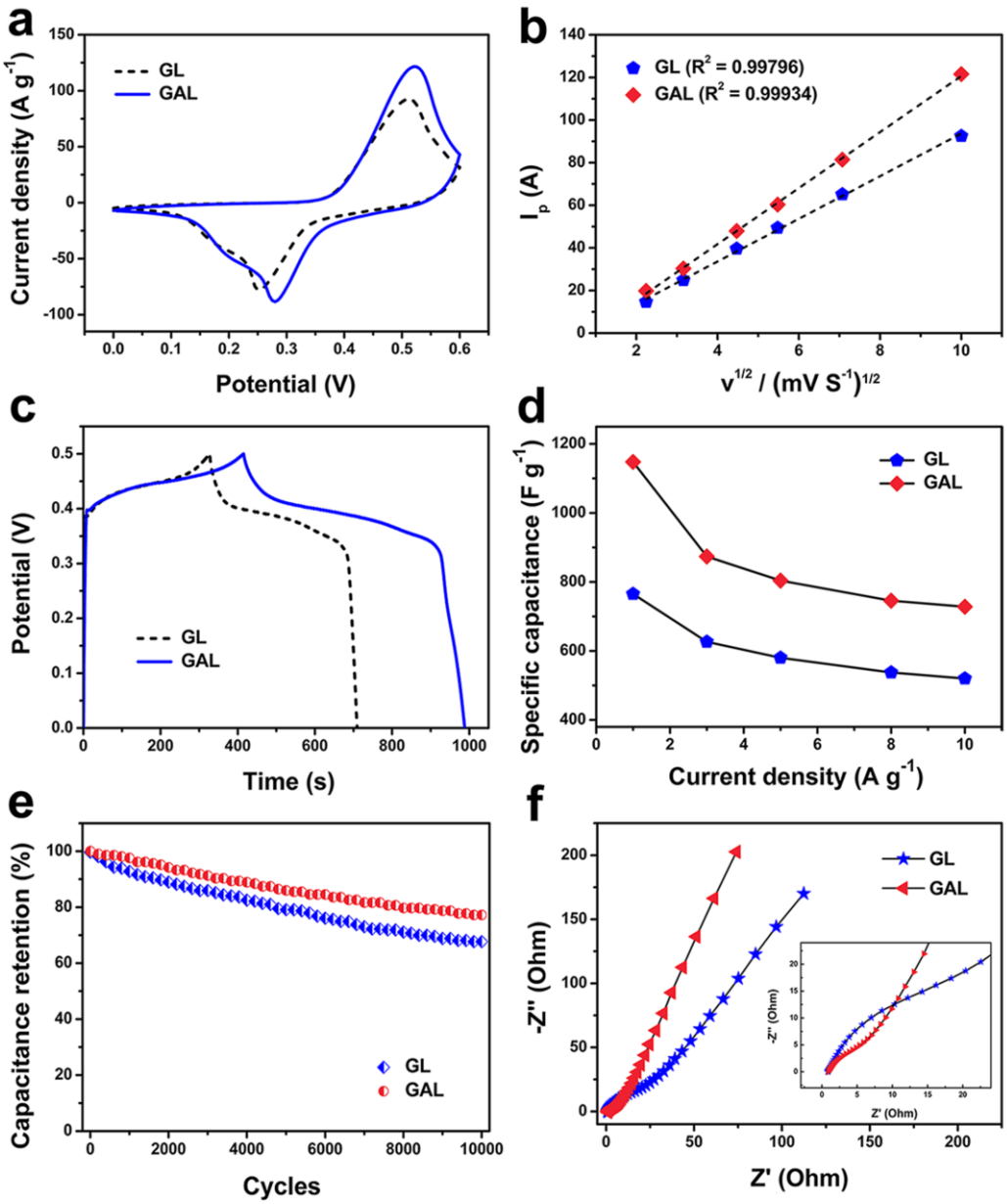

Fig. 5. Electrochemical measurements of the GAL and GL electrodes: (a) CV curves at a scan rate of 100 mV s^{-1}; (b) Linear relationship between the cathodic peak current and square root of the scan rates; (c) GCD curves at a current density of 1 A g^{-1}; (d) Specific capacitances at different current densities; (e) Cycling performances at a current density of 5 A g^{-1}; and (f) Nyquist plots.

Fig. 5c shows the GCD curves of the GAL and GL electrodes at a current density of 1 A g^{-1} with the potential window from 0 V to 0.5 V. The GAL electrode delivers a high specific capacitance of 1148 F g^{-1} at 1 A g^{-1}, which is 1.5 times higher than that of the GL electrode (765.2 F g^{-1} at 1 A g^{-1}). The specific capacitances of the GAL and GL electrodes at different current densities are shown in Fig 5d. The calculated specific capacitances of the GAL electrode are 1148, 873.6, 804, 745.6 and 728 F g^{-1}, whereas the calculated specific capacitances of the GL electrode are 765.2, 626.4, 580, 537.6 and 520 F g^{-1}, at current densities of 1, 3, 5, 8, and 10 A g^{-1}, respectively. Moreover, the GCD curves of the GAL and GL electrodes at various current densities of 1, 3, 5, 8 and 10 A g^{-1} are shown in Fig S4c-d. The GAL electrode exhibits a longer charge/discharge time than GL electrode at all tested current density range, demonstrating the merits of the hierarchical AL composites embedded in the rGO sheet structure. The nonlinear GCD curves represent the typical Faradaic characteristic, indicating the quasi-reversible redox reactions at the electrolyte−electrode interface [59]. Notably, the deviation of the potential range between CV and GCD curves is due to the electrochemical polarization of the materials [67]. The cycling performances of the GAL and GL electrodes were conducted at progressively increased current densities (Fig. S4e). At the first 100 cycles of charge/discharge at a current density of 1 A g^{-1}, the GAL electrode shows a high specific capacitance of 1148 F g^{-1}, whereas the GL electrode shows a specific capacitance of 765.2 F g^{-1}. The specific capacitances of the GAL and GL electrodes show a descending trend with the increase in current density, which can be attributed to the polarization effect of the electrodes [68]. After continuous cycling for 400 cycles at various current densities, the current density is reduced back to 1 A g^{-1}, the GAL electrode retained 98.5% of the initial specific capacitance (1130.8 F g^{-1}) and remained for another 100 cycles constantly. By contrast, the GL electrode maintained 96.2% of the initial capacitance (736.1 F g^{-1}). The cycling performances of the GAL and GL electrodes were evaluated with

repeated charge/discharge testes at a current density of 5 A g^{-1} (Fig. 5e). Remarkably, the GAL electrode exhibits a decent capacitance retention of 77.2% (initial specific capacitance of 886.3 F g^{-1}) and Columbic efficiency of 98.5% after 10000 cycles, which is higher than that of the GL electrode (67.7% decent capacitance retention, initial specific capacitance of 518.1 F g^{-1}; Coulombic efficiency of 91.2%; Fig. S4f). The remarkable electrochemical performances and cycling stability of the GAL electrode are attributed to the rational design of the electrode. The high utilization of electroactive surface area of NiAl LDH nanosheets in the AL composites results in high pseudocapacitance. Meanwhile, the space between AL composites and rGO sheets enables effective penetration of electrolyte ions, which shortens the ions diffusion paths. The rGO sheets significantly protect the NiAl LDH from dissolution in the electrolyte during cycling. In addition, the highly electrically conductive 1D Ag NW core provides rapid electron transport and effectively prevents NiAl LDH from aggregation, leading to high cycling stability.

EIS analysis was used to evaluate the conductivity and charge transfer kinetics of the GAL and GL electrodes (Fig. 5f). The Nyquist plots of the electrodes are depicted at the frequency range from 100 KHz to 0.01 Hz showing a semicircle in the high-frequency region and a sloped line in the low-frequency region. At high frequencies, the intercept at the real part (Z′) indicates the combinational series resistance (R_s) of the electrode, bulk electrolyte, and electrode/current collector contact resistance [69]. The diameter of the semicircle corresponds to the charge transfer resistance (R_{ct}) at the interface between the electrode material and electrolyte. The R_s was measured to be 0.62 Ω for the GAL film electrode and 0.96 Ω for the GL electrode; thus, the GAL film electrode has a higher electrical conductivity attributed to the1D core Ag NWs. The GAL film electrode also displays a smaller R_{ct} (4.68 Ω) compared with the GL electrode (16.72 Ω) at the high-frequency region, indicating a faster electron

transfer process [70]. In addition, the straight line in the low-frequency region corresponds to the Warburg resistance (Z_w). Meanwhile, the GAL film electrode depicts a steeper slope line at the low-frequency region, suggesting the high ion diffusion in the electrode materials. The results demonstrate that the GAL film electrode possesses superior electrical conductivity and effective charge transfer kinetics.

Fig. 6a displays the schematic of the GAL//GAL AFSC device assembled using GAL thin films as the positive and negative electrodes with PVA-KOH as a gel electrolyte. Freestanding GAL possesses high mechanical flexibility, as demonstrated by rolling it on the surface of the stainless-steel rod (Fig. 6b). In this study, Au-PET was used as a substrate of the AFSC due to its mechanical flexibility as demonstrated in the flat and bending conditions of the GAL//GAL AFSC (Fig. 6b and S5**)**. The CV curves of the GAL//GAL AFSC (Fig. 6c) are presented at various scan rates from 5–100 m V s^{-1} between 0 V and 1 V. These quasi-rectangular patterns illustrate the typical Faradaic behavior and the mild distortion is attributed to the oxygen-related functional groups existing on the surface of electrode materials [71]. Fig. 6d shows the GCD curves of the GAL//GAL AFSC with different current densities of 1, 3, 5, 8 and 10 A g^{-1}, respectively. The results reveal the symmetric and nearly triangular shapes with smaller IR drop, indicating the device has ideal capacitive behavior and lower internal resistance. The specific capacitances of the GAL//GAL AFSC are calculated to be 127.2, 99.6, 84, 68.8 and 60 F g^{-1} at current densities of 1, 3, 5, 8 and 10 A g^{-1}, respectively (Fig. 6e). Cycling performance is one of the important parameters to evaluate the practical application for energy storage device. As shown in Fig. 6f, the GAL//GAL AFSC exhibits excellent cycling stability of 83.2 % capacitance retention after 10000 cycles at a current density of 5 A g^{-1}, suggesting superior electrochemical stability of proposed GAL electrode structure. In addition, the coulombic efficiency of the GAL//GAL

AFSC remains at 89.4% at the end of 10000 cycles, demonstrating a remarkable reversibility [60].

To further evaluate the mechanical flexibility of the device, the CV curves of GAL//GAL AFSC were measured at various bending angles of 0°, 30°, 60°, and 90° (Fig. 7a). The corresponding CV and CD curves (Fig. 7b-c) maintain the same shape without a significant difference at all tested bending angles, suggesting the excellent flexibility and electrochemical performance of the device. Meanwhile, the mechanical fatigue tests of the device were also investigated by CV and CD measurements at the repeated bending tests (Fig. 7e-f). After 100 cycles of bending to 90^{o}, the GAL//GAL AFSC retained 93.1 % initial capacitance. The slight decrease of the specific capacitance during bending is attributed to the loss of the adhesion ability of the AFSC device during bending cycles [72].

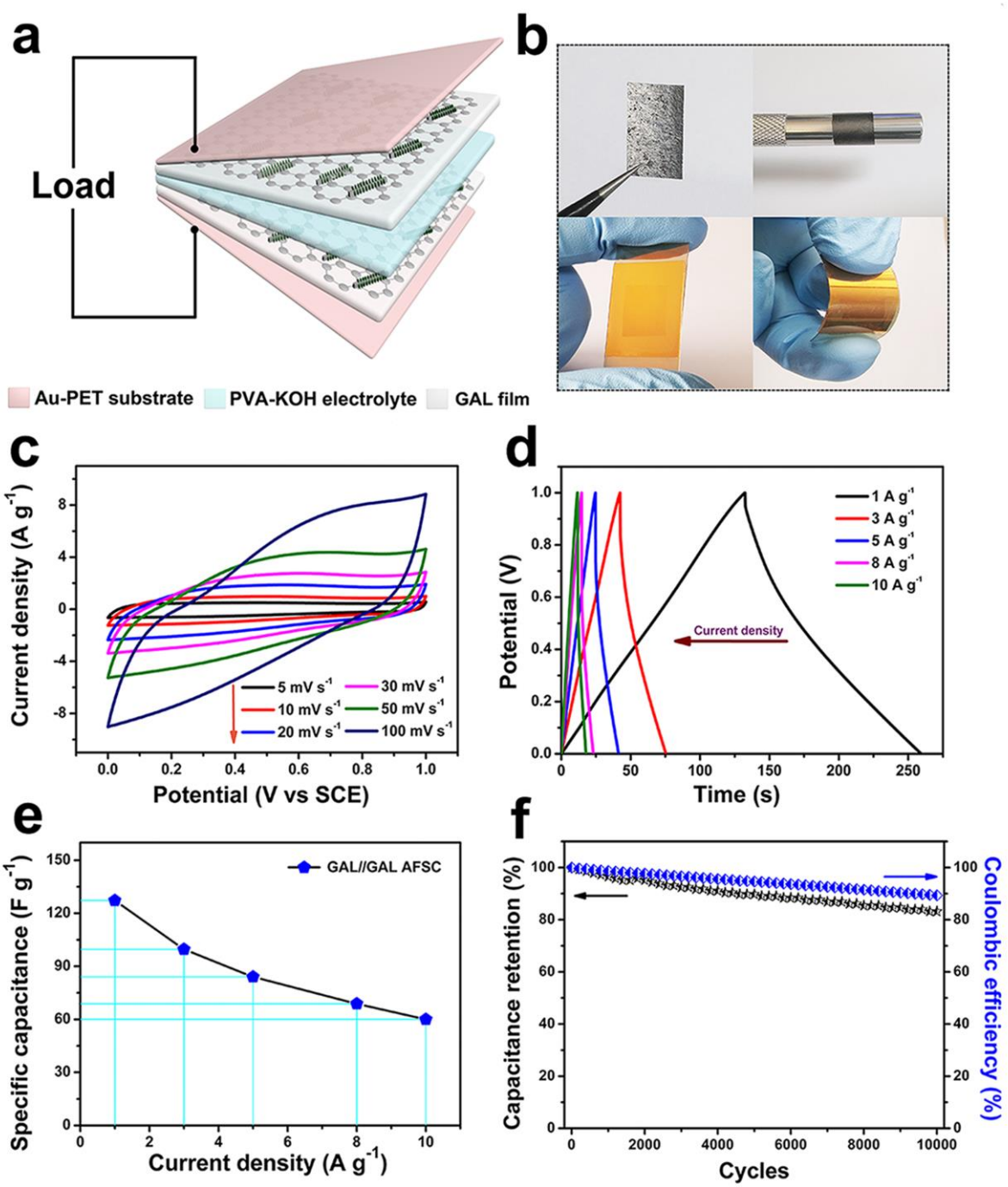

Fig. 6. (a) Schematic illustration of the GAL//GAL AFSC device; (b) Photographic images of the GAL film and AFSC device. Electrochemical measurements of the GAL//GAL AFSC device: (c) CV curves at different scan rates, (d) GCD curves at various current densities, (e) Specific capacitances at different current densities, and (f) Cycling performance and Coulombic efficiency at a current density of 5 A g^{-1}.

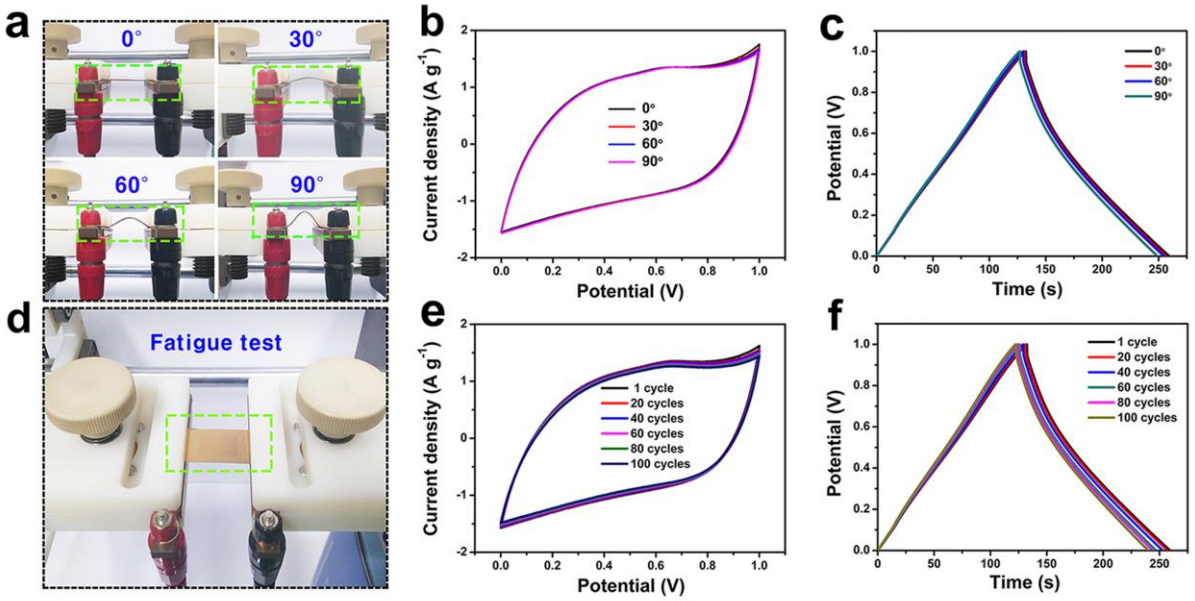

Fig. 7. (a) Photographic image, (b) CV and (c) GCD curves of GAL//GAL AFSC device at various bending angles; (d) Photographic image of the mechanical fatigue tests; (e) CV and (f) GCD curves of GAL//GAL AFSC device at different bending cycles.

The mass energy density and power densities of the GAL//GAL AFSC device were calculated and shown on the Ragone plot (Fig. S6). In this figure, the GAL//GAL AFSC device displays a satisfactory mass energy density of 17.7 Wh kg^{-1} at a power density of 500 W kg^{-1}, which is higher than similar symmetric flexible supercapacitors in the literature (Table S1), such as CNT//CNT (5.2 Wh kg^{-1} at 110 W kg^{-1}) [73], Ag NWs/G//Ag NWs/G (4.5 Wh kg^{-1} at 5040 W kg^{-1}) [72], RuO_2/G//RuO_2/G (13 Wh kg^{-1} at 2100 W kg^{-1}) [74], V_2O_5/rGO//V_2O_5/rGO (8.5 Wh kg^{-1} at 425 W kg^{-1}) [75] and G/MnO_2/CNT//G/MnO_2/CNT (8.9 Wh kg^{-1} at 106 W kg^{-1}) [76]. Furthermore, the volumetric energy and power density of the GAL//GAL AFSC device are also evaluated in Fig. 8, which delivered excellent performance of 35.75 mWh cm^{-3} and 1.01 W cm^{-3}. The detail comparison of the volumetric energy and power densities is shown in Table S2. Notably, our results are superior to many recently reports, such as G/AC//G/AC (15.9 mWh cm^{-3} at 0.0236 W cm^{-3}) [77],

CF/NiP_x//CF/rGO (8.97 mWh cm^{-3} at 0.07 W cm^{-3}) [78], CNT/rGO//CNT/rGO (6.3 mWh cm^{-3} at 0.015 W cm^{-3}) [79], G/MoS_2//G/MoS_2 (1.7 mWh cm^{-3} at 0.062 W cm^{-3}) [80], Mn_3O_4/rGO//Mn_3O_4/rGO (18 mWh cm^{-3} at 3.13 W cm^{-3}) [81], CNTs/$NiCo_2O_4$//CNTs/$NiCo_2O_4$ (1.17 mWh cm^{-3} at 2.43 W cm^{-3}) [82], CF/rGO/MnO_2//CF/rGO (1.23 mWh cm^{-3} at 0.03 W cm^{-3}) [83] and CNF/rGO/MoO_xN_y// CNF/rGO/MoO_xN_y (18.8 mWh cm^{-3} at 0.016 W cm^{-3}) [84].

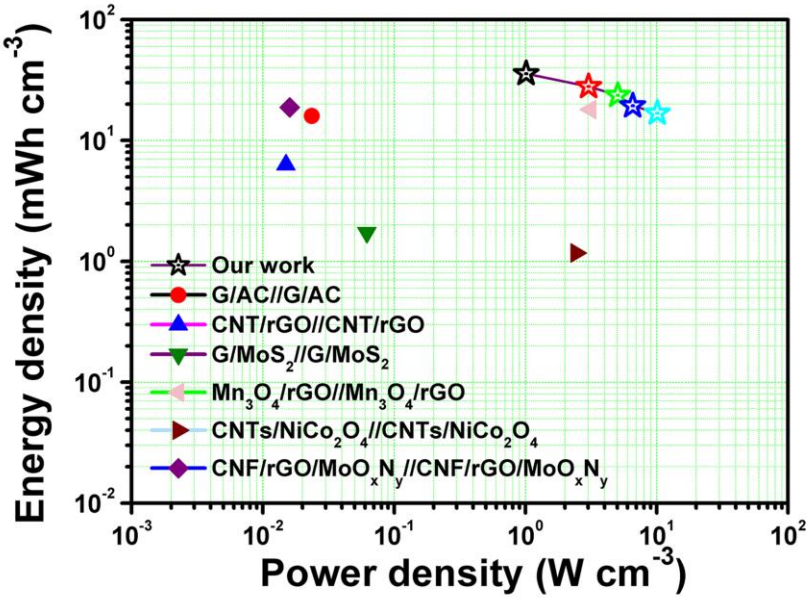

Fig. 8. Volumetric energy and power densities of GAL//GAL AFSC device, and compared with several similar reports.

Conclusions

In summary, we reported a novel flexible GAL film electrode composed of AL composites and rGO sheets by facial hydrothermal and vacuum filtration approaches. Specifically, the hierarchical core-shell structure of AL composites was prepared by grafting NiAl LDH nanosheets vertically on 1D Ag NWs by a facile hydrothermal method. The GAL hybrid film electrode was fabricated by the electrostatic attraction of AL composites and rGO nanosheets

by vacuum filtration technique. The GAL electrode shows superior electrochemical performance with specific capacitance of 1148 F g^{-1} at 1 A g^{-1} and prominent cycling stability of 77.2% after 10000 cycles. Furthermore, the GAL//GAL AFSC device was assembled using GAL electrodes as positive and negative electrodes and PVA-KOH gel as the solid-state electrolyte. The GAL//GAL AFSC device exhibits outstanding flexibility and great stability. A high volumetric energy density of 35.75 mWh cm^{-3} at a power density of 1.01 W cm^{-3} was achieved with remarkable cycling stability of 89.4% after 10000 cycles. This study presents a promising flexible electrode structure with high electrochemical performance and stability for high-performance flexible energy storage devices.

Acknowledgements

This work was supported by the Basic Science Research Program through the National Research Foundation (NRF) funded by the Korea Ministry of Education [2016R1D1A1B02009234]; the Science and Technology Development Fund of the Macau SAR [FDCT-098/2015/A3]; the Multi-Year Research Grants from the Research & Development Office at the University of Macau [MYRG2017-00216-FST], and the UEA funding.

References

[1] G. Nagaraju, G.S.R. Raju, Y.H. Ko, J.S. Yu, Hierarchical Ni-Co layered double hydroxide nanosheets entrapped on conductive textile fibers: a cost-effective and flexible electrode for high-performance pseudocapacitors, Nanoscale 8 (2016) 812-825.

[2] J.W. Zhao, J. Chen, S.M. Xu, M.F. Shao, Q. Zhang, F. Wei, J. Ma, M. Wei, D.G. Evans, X. Duan, Hierarchical NiMn Layered Double Hydroxide/Carbon Nanotubes Architecture with Superb Energy Density for Flexible Supercapacitors, Adv. Funct. Mater. 24 (2014) 2938-2946.

[3] J.L. Liu, L.L. Zhang, H.B. Wu, J.Y. Lin, Z.X. Shen, X.W. Lou, High-performance flexible asymmetric supercapacitors based on a new graphene foam/carbon nanotube hybrid film, Energy Environ. Sci. 7 (2014) 3709-3719.

[4] Q. Xue, J. Sun, Y. Huang, M. Zhu, Z. Pei, H. Li, Y. Wang, N. Li, H. Zhang, C. Zhi, Recent Progress on Flexible and Wearable Supercapacitors, Small 13 (2017) 1701827.
[5] Y. Huang, W.S. Ip, Y.Y. Lau, J. Sun, J. Zeng, N.S.S. Yeung, W.S. Ng, H. Li, Z. Pei, Q. Xue, Weavable, Conductive Yarn-Based NiCo//Zn Textile Battery with High Energy Density and Rate Capability, ACS nano 11 (2017) 8953-8961.
[6] X. Dong, L. Wang, D. Wang, C. Li, J. Jin, Layer-by-layer engineered Co-Al hydroxide nanosheets/graphene multilayer films as flexible electrode for supercapacitor, Langmuir 28 (2011) 293-298.
[7] B.Y. Guan, Y. Yu, X. Wang, S.Y. Song, X.W. Lou, Formation of Onion-Like $NiCo_2S_4$ Particles via Sequential Ion-Exchange for Hybrid Supercapacitors, Adv. Mater. 29 (2017) 1605051.
[8] Y. Huang, M. Zhu, Y. Huang, Z. Pei, H. Li, Z. Wang, Q. Xue, C. Zhi, Multifunctional energy storage and conversion devices, Adv. Mater. 38 (2016) 8344-8364.
[9] G.X. Qu, J.L. Cheng, X.D. Li, D.M. Yuan, P.N. Chen, X.L. Chen, B. Wang, H.S. Peng, A Fiber Supercapacitor with High Energy Density Based on Hollow Graphene/Conducting Polymer Fiber Electrode, Adv. Mater. 28 (2016) 3646-3652.
[10] X.H. Cao, C.L. Tan, X. Zhang, W. Zhao, H. Zhang, Solution-Processed Two-Dimensional Metal Dichalcogenide-Based Nanomaterials for Energy Storage and Conversion, Adv. Mater. 28 (2016) 6167-6196.
[11] M.S. Zhu, Y. Huang, Q.H. Deng, J. Zhou, Z.X. Pei, Q. Xue, Y. Huang, Z.F. Wang, H.F. Li, Q. Huang, C.Y. Zhi, Highly Flexible, Freestanding Supercapacitor Electrode with Enhanced Performance Obtained by Hybridizing Polypyrrole Chains with MXene, Adv. Energy Mater. 6 (2016) 1600969.
[12] M. Huang, F. Li, F. Dong, Y.X. Zhang, L.L. Zhang, MnO_2-based nanostructures for high-performance supercapacitors, J. Mater. Chem. A 3 (2015) 21380-21423.
[13] Z.Y. Zhang, F. Xiao, S. Wang, Hierarchically structured MnO_2/graphene/carbon fiber and porous graphene hydrogel wrapped copper wire for fiber-based flexible all-solid-state asymmetric supercapacitors, J. Mater. Chem. A 3 (2015) 11215-11223.
[14] J.W. Liu, J. Essner, J. Li, Hybrid Supercapacitor Based on Coaxially Coated Manganese Oxide on Vertically Aligned Carbon Nanofiber Arrays, Chem. Mater. 22 (2010) 5022-5030.
[15] C. Choi, J.A. Lee, A.Y. Choi, Y.T. Kim, X. Lepro, M.D. Lima, R.H. Baughman, S.J. Kim, Flexible Supercapacitor Made of Carbon Nanotube Yarn with Internal Pores, Adv. Mater. 26 (2014) 2059-2065.
[16] Y. Huang, M. Zhong, F. Shi, X. Liu, Z. Tang, Y. Wang, Y. Huang, H. Hou, X. Xie, C. Zhi, An Intrinsically Stretchable and Compressible Supercapacitor Containing a Polyacrylamide Hydrogel Electrolyte, Angew. Chem. 56 (2017) 9141-9145.
[17] Y.M. He, W.J. Chen, X.D. Li, Z.X. Zhang, J.C. Fu, C.H. Zhao, E.Q. Xie, Freestanding Three-Dimensional Graphene/MnO_2 Composite Networks As Ultra light and Flexible Supercapacitor Electrodes, Acs Nano 7 (2013) 174-182.
[18] Z.Y. Xiong, C.L. Liao, W.H. Han, X.G. Wang, Mechanically Tough Large-Area Hierarchical Porous Graphene Films for High-Performance Flexible Supercapacitor Applications, Adv. Mater. 27 (2015) 4469-4475.
[19] Z. Zhang, K. Chi, F. Xiao, S. Wang, Advanced solid-state asymmetric supercapacitors based on 3D graphene/MnO_2 and graphene/polypyrrole hybrid architectures, J. Mater. Chem. A 3 (2015) 12828-12835.
[20] Z.-D. Huang, B. Zhang, S.-W. Oh, Q.-B. Zheng, X.-Y. Lin, N. Yousefi, J.-K. Kim, Self-assembled reduced

graphene oxide/carbon nanotube thin films as electrodes for supercapacitors, J. Mater. Chem. 22 (2012) 3591-3599.
[21] Y. Xu, Z. Lin, X. Huang, Y. Liu, Y. Huang, X. Duan, Flexible solid-state supercapacitors based on three-dimensional graphene hydrogel films, ACS nano 7 (2013) 4042-4049.
[22] C. Yu, C. Masarapu, J. Rong, B. Wei, H. Jiang, Stretchable supercapacitors based on buckled single-walled carbon-nanotube macrofilms, Adv. Mater. 21 (2009) 4793-4797.
[23] C. Merlet, B. Rotenberg, P.A. Madden, P.L. Taberna, P. Simon, Y. Gogotsi, M. Salanne, On the molecular origin of supercapacitance in nanoporous carbon electrodes, Nat. Mater. 11 (2012) 306-310.
[24] M. Salanne, B. Rotenberg, K. Naoi, K. Kaneko, P.L. Taberna, C.P. Grey, B. Dunn, P. Simon, Efficient storage mechanisms for building better supercapacitors, Nat. Energy 1 (2016) 16070-16080.
[25] Y. He, W. Chen, X. Li, Z. Zhang, J. Fu, C. Zhao, E. Xie, Freestanding three-dimensional graphene/MnO_2 composite networks as ultralight and flexible supercapacitor electrodes, ACS nano 7 (2012) 174-182.
[26] Y. Cheng, S. Lu, H. Zhang, C.V. Varanasi, J. Liu, Synergistic effects from graphene and carbon nanotubes enable flexible and robust electrodes for high-performance supercapacitors, Nano Lett. 12 (2012) 4206-4211.
[27] Z.Y. Zhang, F. Xiao, L.H. Qian, J.W. Xiao, S. Wang, Y.Q. Liu, Facile Synthesis of 3D MnO_2-Graphene and Carbon Nanotube-Graphene Composite Networks for High-Performance, Flexible, All-Solid-State Asymmetric Supercapacitors, Adv. Energy Mater. 4 (2014) 1400064.
[28] Y.F. Zhao, H.N. Ma, S.F. Huang, X.J. Zhang, M.R. Xia, Y.F. Tang, Z.F. Ma, Monolayer Nickel Cobalt Hydroxyl Carbonate for High Performance All-Solid-State Asymmetric Supercapacitors, ACS Appl. Mater. Interfaces 8 (2016) 22997-23005.
[29] Z. Zhang, F. Xiao, Y. Guo, S. Wang, Y. Liu, One-pot self-assembled three-dimensional TiO_2-graphene hydrogel with improved adsorption capacities and photocatalytic and electrochemical activities, ACS Appl. Mater. Interfaces 5 (2013) 2227-2233.
[30] J.H. Seo, I. Hwang, H.D. Um, S. Lee, K. Lee, J. Park, H. Shin, T.H. Kwon, S.J. Kang, K. Seo, Cold Isostatic-Pressured Silver Nanowire Electrodes for Flexible Organic Solar Cells via Room-Temperature Processes, Adv. Mater. 29 (2017) 1701479.
[31] H. Kang, Y. Kim, S. Cheon, G.-R. Yi, J.H. Cho, Halide Welding for Silver Nanowire Network Electrode, ACS Appl. Mater. Interfaces 9 (2017) 30779-30785.
[32] J. Chen, H. Bi, S. Sun, Y. Tang, W. Zhao, T. Lin, D. Wan, F. Huang, X. Zhou, X. Xie, Highly conductive and flexible paper of 1D silver-nanowire-doped graphene, ACS Appl. Mater. Interfaces 5 (2013) 1408-1413.
[33] L. Li, K.S. Hui, K.N. Hui, Y.R. Cho, Ultrathin petal-like NiAl layered double oxide/sulfide composites as an advanced electrode for high-performance asymmetric supercapacitors, J. Mater. Chem. A 5 (2017) 19687-19696.
[34] L. Zhang, R. Chen, K.N. Hui, K.S. Hui, H. Lee, Hierarchical ultrathin NiAl layered double hydroxide nanosheet arrays on carbon nanotube paper as advanced hybrid electrode for high performance hybrid capacitors, Chem. Eng. J. 325 (2017) 554-563.
[35] L.J. Zhang, J. Wang, J.J. Zhu, X.G. Zhang, K.S. Hui, K.N. Hui, 3D porous layered double hydroxides grown on graphene as advanced electrochemical pseudocapacitor materials, J. Mater. Chem. A 1 (2013) 9046-9053.

[36] M. Li, F. Liu, J.P. Cheng, J. Ying, X.B. Zhang, Enhanced performance of nickel-aluminum layered double hydroxide nanosheets/carbon nanotubes composite for supercapacitor and asymmetric capacitor, J. Alloys Compd. 635 (2015) 225-232.
[37] F. He, Z. Hu, K. Liu, S. Zhang, H. Liu, S. Sang, In situ fabrication of nickel aluminum-layered double hydroxide nanosheets/hollow carbon nanofibers composite as a novel electrode material for supercapacitors, J. Power Sources 267 (2014) 188-196.
[38] J. Chen, H. Bi, S.R. Sun, Y.F. Tang, W. Zhao, T.Q. Lin, D.Y. Wan, F.Q. Huang, X.D. Zhou, X.M. Xie, M.H. Jiang, Highly Conductive and Flexible Paper of 1D Silver-Nanowire-Doped Graphene, ACS Appl. Mater. Interfaces 5 (2013) 1408-1413.
[39] J. Jiu, T. Araki, J. Wang, M. Nogi, T. Sugahara, S. Nagao, H. Koga, K. Suganuma, E. Nakazawa, M. Hara, H. Uchida, K. Shinozaki, Facile synthesis of very-long silver nanowires for transparent electrodes, J. Mater. Chem. A 2 (2014) 6326-6330.
[40] S. Hu, T. Han, C. Lin, W. Xiang, Y. Zhao, P. Gao, F. Du, X. Li, Y. Sun, Enhanced Electrocatalysis via 3D Graphene Aerogel Engineered with a Silver Nanowire Network for Ultrahigh-Rate Zinc-Air Batteries, Adv. Funct. Mater. 27 (2017) 1700041.
[41] L.J. Zhang, K.N. Hui, K.S. Hui, X. Chen, R. Chen, H. Lee, Role of graphene on hierarchical flower-like NiAl layered double hydroxide-nickel foam-graphene as binder-free electrode for high-rate hybrid supercapacitor (vol 41, pg 9443, 2016), Int. J. Hydrogen Energy 41 (2016) 13329-13329.
[42] S. Wu, K. Hui, K. Hui, One-Dimensional Core-Shell Architecture Composed of Silver Nanowire@ Hierarchical Nickel-Aluminum Layered Double Hydroxide Nanosheet as Advanced Electrode Materials for Pseudocapacitor, J. Phys. Chem. C 119 (2015) 23358-23365.
[43] Y. Sun, J. Tang, K. Zhang, J. Yuan, J. Li, D.-M. Zhu, K. Ozawa, L.-C. Qin, Comparison of reduction products from graphite oxide and graphene oxide for anode applications in lithium-ion batteries and sodium-ion batteries, Nanoscale 9 (2017) 2585-2595.
[44] H. Zhao, K.S. Hui, K.N. Hui, Synthesis of nitrogen-doped multilayer graphene from milk powder with melamine and their application to fuel cells, Carbon 76 (2014) 1-9.
[45] J. Yan, C.E. Ren, K. Maleski, C.B. Hatter, B. Anasori, P. Urbankowski, A. Sarycheva, Y. Gogotsi, Flexible MXene/graphene films for ultrafast supercapacitors with outstanding volumetric capacitance, Adv. Funct. Mater. 27 (2017) 1701264.
[46] B. Hwang, C.-H. An, S. Becker, Highly robust Ag nanowire flexible transparent electrode with UV-curable polyurethane-based overcoating layer, Mater. Des. 129 (2017) 180-185.
[47] L. Zhang, R. Chen, K.N. Hui, K. San Hui, H. Lee, Hierarchical ultrathin NiAl layered double hydroxide nanosheet arrays on carbon nanotube paper as advanced hybrid electrode for high performance hybrid capacitors, Chem. Eng. J. 325 (2017) 554-563.
[48] S.C. Sekhar, G. Nagaraju, J.S. Yu, Conductive silver nanowires-fenced carbon cloth fibers-supported layered double hydroxide nanosheets as a flexible and binder-free electrode for high-performance asymmetric supercapacitors, Nano Energy 36 (2017) 58-67.
[49] L. Zhang, J. Wang, J. Zhu, X. Zhang, K. San Hui, K.N. Hui, 3D porous layered double hydroxides grown on graphene as advanced electrochemical pseudocapacitor materials, J. Mater. Chem. A 1 (2013) 9046-9053.

[50] H.B. Feng, R. Cheng, X. Zhao, X.F. Duan, J.H. Li, A low-temperature method to produce highly reduced graphene oxide, Nat. Commun. 4 (2013) 1539.
[51] Q.D. Cheng, S. Gong, Q. Zhang, R. Wang, L. Jiang, Synergistically toughening nacre-like graphene nanocomposites via gel-film transformation, J. Mater. Chem. A 5 (2017) 16386-16392.
[52] S. Yue, H. Tong, Z. Gao, W. Bai, L. Lu, J. Wang, X. Zhang, Fabrication of flexible nanoporous nitrogen-doped graphene film for high-performance supercapacitors, J. Solid State Electrochem. 21 (2017) 1653-1663.
[53] R.Z. Ma, Z.P. Liu, L. Li, N. Iyi, T. Sasaki, Exfoliating layered double hydroxides in formamide: a method to obtain positively charged nanosheets, J. Mater. Chem. 16 (2006) 3809-3813.
[54] D. Li, M.B. Muller, S. Gilje, R.B. Kaner, G.G. Wallace, Processable aqueous dispersions of graphene nanosheets, Nat. Nanotechnol 3 (2008) 101-105.
[55] C.S. Rout, P.D. Joshi, R.V. Kashid, D.S. Joag, M.A. More, A.J. Simbeck, M. Washington, S.K. Nayak, D.J. Late, Superior field emission properties of layered WS_2-RGO nanocomposites, Sci. Rep. 3 (2013) 3282.
[56] Y. Chen, X.O. Zhang, D.C. Zhang, P. Yu, Y.W. Ma, High performance supercapacitors based on reduced graphene oxide in aqueous and ionic liquid electrolytes, Carbon 49 (2011) 573-580.
[57] J.T. Zhang, J.W. Jiang, H.L. Li, X.S. Zhao, A high-performance asymmetric supercapacitor fabricated with graphene-based electrodes, Energy Environ. Sci. 4 (2011) 4009-4015.
[58] Y. Wei, S. Chen, Y. Lin, X. Yuan, L. Liu, Silver nanowires coated on cotton for flexible pressure sensors, J. Mater. Chem. C 4 (2016) 935-943.
[59] G.K. Veerasubramani, A. Chandrasekhar, M. Sudhakaran, Y.S. Mok, S.J. Kim, Liquid electrolyte mediated flexible pouch-type hybrid supercapacitor based on binderless core-shell nanostructures assembled with honeycomb-like porous carbon, J. Mater. Chem. A 5 (2017) 11100-11113.
[60] S.X. Wu, K.S. Hui, K.N. Hui, K.H. Kim, Electrostatic-Induced Assembly of Graphene-Encapsulated Carbon@Nickel-Aluminum Layered Double Hydroxide Core-Shell Spheres Hybrid Structure for High-Energy and High-Power-Density Asymmetric Supercapacitor, ACS Appl. Mater. Interfaces 9 (2017) 1395-1406.
[61] H. Chen, L.F. Hu, M. Chen, Y. Yan, L.M. Wu, Nickel-Cobalt Layered Double Hydroxide Nanosheets for High- performance Supercapacitor Electrode Materials, Adv. Funct. Mater. 24 (2014) 934-942.
[62] D. Du, X. Wu, S. Li, Y. Zhang, W. Xing, L. Li, Q. Xue, P. Bai, Z. Yan, Remarkable supercapacitor performance of petal-like LDHs vertically grown on graphene/polypyrrole nanoflakes, J. Mater. Chem. A 5 (2017) 8964-8971.
[63] Q. Sun, J. Liu, X. Li, B. Wang, H. Yadegari, A. Lushington, M.N. Banis, Y. Zhao, W. Xiao, N. Chen, Atomic Layer Deposited Non-Noble Metal Oxide Catalyst for Sodium-Air Batteries: Tuning the Morphologies and Compositions of Discharge Product, Adv. Funct. Mater. 27 (2017) 1606662.
[64] J. Xu, S.L. Gai, F. He, N. Niu, P. Gao, Y.J. Chen, P.P. Yang, A sandwich-type three-dimensional layered double hydroxide nanosheet array/graphene composite: fabrication and high supercapacitor performance, J. Mater. Chem. A 2 (2014) 1022-1031.
[65] S. Liu, K.S. Hui, K.N. Hui, Flower-like Copper Cobaltite Nanosheets on Graphite Paper as High-Performance Supercapacitor Electrodes and Enzymeless Glucose Sensors, ACS Appl. Mater. Interfaces 8 (2016) 3258-3267.
[66] S.G. Krishnan, M. Reddy, M. Harilal, B. Vidyadharan, I.I. Misnon, M.H. Ab Rahim, J. Ismail, R. Jose,

Characterization of $MgCo_2O_4$ as an electrode for high performance supercapacitors, Electrochim. Acta 161 (2015) 312-321.
[67] Q.X. Xia, K.S. Hui, K.N. Hui, S.D. Kim, J.H. Lim, S.Y. Choi, L.J. Zhang, R.S. Mane, J.M. Yun, K.H. Kim, Facile synthesis of manganese carbonate quantum dots/$Ni(HCO_3)_2$-$MnCO_3$ composites as advanced cathode materials for high energy density asymmetric supercapacitors, J. Mater. Chem. A 3 (2015) 22102-22117.
[68] H. Lai, Q. Wu, J. Zhao, L. Shang, H. Li, R. Che, Z. Lyu, J. Xiong, L. Yang, X. Wang, Mesostructured NiO/Ni composites for high-performance electrochemical energy storage, Energy Environ. Sci. 9 (2016) 2053-2060.
[69] B. Wang, Q. Liu, Z.Y. Qian, X.F. Zhang, J. Wang, Z.S. Li, H.J. Yan, Z. Gao, F.B. Zhao, L.H. Liu, Two steps in situ structure fabrication of Ni-Al layered double hydroxide on Ni foam and its electrochemical performance for supercapacitors, J. Power Sources 246 (2014) 747-753.
[70] F.L. Lai, Y.E. Miao, Y.P. Huang, T.S. Chung, T.X. Liu, Flexible Hybrid Membranes of $NiCo_2O_4$-Doped Carbon Nanofiber@MnO_2 Core-Sheath Nanostructures for High-Performance Supercapacitors, J. Phys. Chem. C 119 (2015) 13442-13450.
[71] J.A. Syed, J. Ma, B. Zhu, S. Tang, X. Meng, Hierarchical Multicomponent Electrode with Interlaced Ni $(OH)_2$ Nanoflakes Wrapped Zinc Cobalt Sulfide Nanotube Arrays for Sustainable High-Performance Supercapacitors, Adv. Energy Mater. 7 (2017) 1701228.
[72] J. Zhi, W. Zhao, X. Liu, A. Chen, Z. Liu, F. Huang, Highly conductive ordered mesoporous carbon based electrodes decorated by 3D graphene and 1D silver nanowire for flexible supercapacitor, Adv. Funct. Mater. 24 (2014) 2013-2019.
[73] C.J. Yu, C. Masarapu, J.P. Rong, B.Q. Wei, H.Q. Jiang, Stretchable Supercapacitors Based on Buckled Single-Walled Carbon Nanotube Macrofilms, Adv. Mater. 21 (2009) 4793.
[74] S. Cho, J. Kim, Y. Jo, A.T.A. Ahmed, H. Chavan, H. Woo, A. Inamdar, J. Gunjakar, S. Pawar, Y. Park, Bendable RuO_2/graphene thin film for fully flexible supercapacitor electrodes with superior stability, J. Alloys Compd. 725 (2017) 108-114.
[75] S.D. Perera, M. Rudolph, R.G. Mariano, N. Nijem, J.P. Ferraris, Y.J. Chabal, K.J. Balkus, Manganese oxide nanorod-graphene/vanadium oxide nanowire-graphene binder-free paper electrodes for metal oxide hybrid supercapacitors, Nano Energy 2 (2013) 966-975.
[76] Y.W. Cheng, S.T. Lu, H.B. Zhang, C.V. Varanasi, J. Liu, Synergistic Effects from Graphene and Carbon Nanotubes Enable Flexible and Robust Electrodes for High-Performance Supercapacitors, Nano Lett. 12 (2012) 4206-4211.
[77] C. Zheng, X. Zhou, H. Cao, G. Wang, Z. Liu, Synthesis of porous graphene/activated carbon composite with high packing density and large specific surface area for supercapacitor electrode material, J. power sources 258 (2014) 290-296.
[78] Z. Zhang, S. Liu, J. Xiao, S. Wang, Fiber-based multifunctional nickel phosphide electrodes for flexible energy conversion and storage, J. Mater. Chem. A 4 (2016) 9691-9699.
[79] D. Yu, K. Goh, H. Wang, L. Wei, W. Jiang, Q. Zhang, L. Dai, Y. Chen, Scalable synthesis of hierarchically structured carbon nanotube-graphene fibres for capacitive energy storage, Nat. nanotechnology 9 (2014) 555-562.

[80] N. Li, T. Lv, Y. Yao, H. Li, K. Liu, T. Chen, Compact graphene/MoS_2 composite films for highly flexible and stretchable all-solid-state supercapacitors, J. Mater. Chem. A 5 (2017) 3267-3273.
[81] T. Xiong, W.S.V. Lee, X. Huang, J. Xue, Mn_3O_4/Reduced graphene oxide based supercapacitor with ultra-long cyclic performance, Journal of Materials Chemistry A 5 (2017) 12762-12768.
[82] Y. Zheng, Z. Lin, W. Chen, B. Liang, H. Du, R. Yang, X. He, Z. Tang, X. Gui, Flexible, sandwich-like CNTs/$NiCo_2O_4$ hybrid paper electrodes for all-solid state supercapacitors, J. Mater. Chem. A 5 (2017) 5886-5894.
[83] Z. Zhang, F. Xiao, J. Xiao, S. Wang, Functionalized carbonaceous fibers for high performance flexible all-solid-state asymmetric supercapacitors, J. Mater. Chem. A 3 (2015) 11817-11823.
[84] Q. Zheng, A. Kvit, Z. Cai, Z. Ma, S. Gong, A freestanding cellulose nanofibril-reduced graphene oxide-molybdenum oxynitride aerogel film electrode for all-solid-state supercapacitors with ultrahigh energy density, J. Mater. Chem. A 5 (2017) 12528-12541.

Figure captions

Fig. 1. (a) Schematic illustration of the formation process of the hierarchical core-shell AL composites; (b) XRD patterns of NiAl LDH and AL composites; SEM images of (c) Ag NWs and (d) AL composites.

Fig. 2. (a) Schematic illustration of the GAL film; (b) XRD patterns of rGO and GAL film; (c) Tyndall effect illustration of rGO and AL composites dispersions; SEM and cross-sectional images of (d) rGO and (e) GAL film.

Fig. 3. (a, b, c) TEM images of GAL film with different magnifications; (inset in c) the corresponding SAED pattern of NiAl LDH in AL composites; HRTEM image of (d) GAL, (inset in d) rGO and (e) NiAl LDH; (f) Mapping results of AL composites.

Fig. 4. XPS results of the GAL hybrid film: (a) full spectrum, (b) C 1s, (c) Ni 2p, and (d) Ag 3d.

Fig. 5. Electrochemical measurements of the GAL and GL electrodes: (a) CV curves at a scan rate of 100 mV s^{-1}; (b) Linear relationship between the cathodic peak current and square root of the scan rates; (c) GCD curves at a current density of 1 A g^{-1}; (d) Specific capacitances at different current densities; (e) Cycling performances at a current density of 5

A g^{-1}; and (f) Nyquist plots.

Fig. 6. (a) Schematic illustration of the GAL//GAL AFSC device; (b) Photographic images of the GAL film and AFSC device. Electrochemical measurements of the GAL//GAL AFSC device: (c) CV curves at different scan rates, (d) GCD curves at various current densities, (e) Specific capacitances at different current densities, and (f) Cycling performance and Coulombic efficiency at a current density of 5 A g^{-1}.

Fig. 7. (a) Photographic image, (b) CV and (c) GCD curves of GAL//GAL AFSC device at various bending angles; (d) Photographic image of the mechanical fatigue tests; (e) CV and (f) GCD curves of GAL//GAL AFSC device at different bending cycles.

Fig. 8. Volumetric energy and power densities of GAL//GAL AFSC device, and compared with several similar reports.